RSC Advances

PAPER

View Article Online
View Journal | View Issue

Check for updates

Cite this: *RSC Adv.*, 2021, **11**, 39523

Reduction of silver ions in molybdates: elucidation of framework acidity as the factor controlling charge balance mechanisms in aqueous zinc-ion electrolyte†

Derrick Combs,[a] Brendan Godsel,[a] Julie Pohlman-Zordan,[a] Allen Huff,[a] Jackson King,[a] Robert Richter[b] and Paul F. Smith *[a]

A percolating network of high electrical conductivity needed to operate electrodes at a fast rate can be formed by *in situ* reduction of Ag^+ originating from mixed metal oxide lattices, but few studies have elucidated trends in this mechanism as a function of Ag^+ concentration and structure. Candidates compared for the first time here are spinel Ag_2MoO_4, monoclinic and triclinic $Ag_2Mo_2O_7$, and $Ag_2Mo_3O_{10}\cdot 2H_2O$, which have reduction potentials for Ag^+ and Mo^{6+} strongly decoupled by up to ~600 mV in aqueous zinc-ion electrolyte. Under these conditions, Ag^0 is the first reduction product and a decrease of charge transfer resistance by ~100× is observed within 2.5% consumption of total Ag^+ independent of initial structure. However, resistance metrics alone poorly describe materials which are robust to reducing silver with high energy at faster rates. Instead, after accounting for crystallinity and morphology differences, we find that the acidity of the molybdate framework is responsible for a switch in charge balance mechanism from the bulk formation of a mixed $ZnMoO_x$ to pseudocapacitive Zn^{2+} precipitation, and that this mechanism switch is associated with minimized losses to rate, voltage and capacity yields as carbon/binder free electrodes relative to composites. The location of this acidity cutoff near the pH of the $ZnSO_4$ electrolyte may suggest a design principle for future low-carbon electrodes beyond molybdate framework structures.

Received 20th October 2021
Accepted 7th December 2021

DOI: 10.1039/d1ra07765a

rsc.li/rsc-advances

Open Access Article. Published on 13 December 2021. Downloaded on 2/20/2026 2:13:40 PM.
This article is licensed under a Creative Commons Attribution 3.0 Unported Licence.

Introduction

Electrodes must increasingly support faster electron transport as the devices they power become more demanding. Towards this goal, the development of materials containing Ag^+ is pursued for fundamental interest because the reduced product can contain a network of atomically dispersed, conductive Ag^0 particles that support fast electron transport throughout the bulk.[1,2] Minute amounts of dispersed Ag^+ are known to significantly improve electronic transport; as example, cathodes of the silver–vanadium–phosphate-oxide type show percolation thresholds with 0.3% volume reduction of Ag^+ concurrently resulting in 10^6 decrease in electrical resistance.[3–5] Silver vanadium oxide (SVO) cathodes remain the dominant material in implantable cardiac defibrillator batteries due to this reductive displacement mechanism.[6]

Given that vanadium oxide cathodes have shown tremendous promise in aqueous zinc-ion batteries (AZIB's)[7–9] recent efforts to incorporate reductive displacement cathodes in this new application have included Ag^0-doped V_2O_5,[10] $Ag_{0.4}V_2O_5$,[11] $Ag_{1.2}V_3O_8$,[12] $Ag_2V_4O_{11}$,[13] $Ag_{0.33}V_2O_5@V_2O_5\cdot nH_2O$,[14] β-$AgVO_3$,[15] and even Cu analogs in CuV_2O_6,[16,17] $Cu_{0.95}V_2O_5$,[18] $Cu_xV_2O_5$,[19] $Cu_{0.34}V_2O_5$ (ref. 20) and $Cu_3(OH)_2V_2O_7$.[21,22] However, an early emphasis on reporting individual structural metrics – which we summarize in Table S1† – rather than critical comparisons has led to inconsistencies when viewed broadly that, to our knowledge, have not been addressed. Only one study attempts to directly compare any subset of these structures in AZIBs, finding tunneled $Ag_{0.33}V_2O_5$ outperformed layered $Ag_2V_4O_{11}$ and chain-like β-$AgVO_3$ at cycle life, with the latter exhibiting rapid capacity fade to <25 mA h g^{-1} at 1000 mA g^{-1} rates in only 25 cycles.[12,23] With reports that chain-like β-$AgVO_3$ is capable of 95 mA h g^{-1} after 1000 cycles at 2000 mA g^{-1} rates with 78% retention[15] and layered $Ag_2V_4O_{11}$ is capable of 93% capacity retention after 6000 cycles at 5 A g^{-1} rates,[13] it is clear there exist factors as yet unknown which either caused these materials to perform worse in the comparative study or caused them to improve individually. Among many possiblities,[24] sample crystallinity and morphology may rank highly considering that the

[a]*Department of Chemistry, Valparaiso University, 1710 Chapel Drive, Valparaiso, IN 46383, USA. E-mail: paul.smith1@valpo.edu*

[b]*Department of Chemistry and Physics, Chicago State University, 9501 S. King Drive, Chicago, IL 60628, USA*

† Electronic supplementary information (ESI) available: 16 figures and discussion on the synthesis of $Ag_2Mo_3O_{10}\cdot 2H_2O$. See DOI: 10.1039/d1ra07765a

© 2021 The Author(s). Published by the Royal Society of Chemistry

Open Access Article. Published on 13 December 2021. Downloaded on 2/20/2026 2:13:40 PM.
This article is licensed under a Creative Commons Attribution 3.0 Unported Licence.

studies reporting improved metrics from β-$AgVO_3$ and $Ag_2V_4O_{11}$ prepared nanowires and the comparative test did not.

We argue that, irrespective of whether this conjecture is true, it is not needed if a new set of testing conditions is widely adopted for reductive displacement cathodes. After all, these are materials which, at their best, enable their own conductivity and should require electrodes with little (or no) additives, especially when compared to manufactured $LiCoO_2$ and alkaline MnO_2 cathodes with ~86–95% active material.[25–27] In spite of this tremendous advantage, all the aforementioned studies prepared electrodes with as much as 20% carbon and 10% binder. The consequence of this disconnect between the conditions in which SVO's should thrive *vs.* the conditions evaluated is that laudable metrics are reported irrespective of whether the SVO structure is tunneled, layered, or chain-like, and this fact is clearly the major contributor to the above inconsistency. For those in pursuit of structure/function relationships this should not be a satisfactory state of literature, especially considering the presence of Ag^+ does not even guarantee reductive displacement occurs. For instance, lithiation of $Ag_xMn_8O_{16}$ ($1.0 \leq x \leq 1.8$) does not form Ag^0 immediately, but rather Mn accepts the first ~4 electron equivalents.[28,29]

Even with a lower reduction potential, V^{5+} is still competitive with Ag^+ for early electrons in $Ag_2VO_2PO_4$,[1] resulting in Ag^0 networks which may form differently as a function of rate[30] and other factors,[31] including the identity of the intercalating ion. Ag^0 appears immediately when $Ag_xMn_8O_{16}$ is discharged in sodium batteries,[32] and reoxidation of Ag^0 which is not known in lithium batteries occurs in aqueous Zn systems.[33] Clearly, there is a need to better understand reductive displacement mechanisms in AZIBs since these new conditions may establish novel paradigms. A promising system to do so would contain a metal with a strongly decoupled reduction potential from Ag^+.

The Ag_2O–MoO_3 phase diagram contains numerous viable candidates for this including spinel Ag_2MoO_4, layered $Ag_6Mo_{10}O_{33}$, orthorhombic $Ag_2Mo_3O_{10}$, and two $Ag_2Mo_2O_7$ polymorphs.[34–36] $Ag_6Mo_{10}O_{33}$ was reported as a cathode once in 1978 (ref. 37) and more recently has appeared as a topic of study in supercapacitor application.[38] The electrochemistry of monoclinic and triclinic polymorphs of $Ag_2Mo_2O_7$ has recently appeared in separate studies, where the former is capable of 825 mA h g^{-1} at 100 mA g^{-1} rates in lithium ion batteries,[39] and the latter is capable of 190 mA h g^{-1} at 20 mA g^{-1} rates in sodium ion batteries.[40] Collectively, these reports represent the entire body of research on the electrochemistry of silver molybdenum oxides (SMOs) at present knowledge.

Here, we find a subset of four SMO's (Ag_2MoO_4, monoclinic and triclinic $Ag_2Mo_2O_7$ and $Ag_2Mo_3O_{10}\cdot 2H_2O$) which all reduce in absence of additives to form Ag^0 early in discharge (0.05 electrons) yielding electrodes with lowered resistance by ~100× and within an order of magnitude of each other. Even with this property, the electrodes show different capabilities to deliver voltage, capacity, and energy as a function of rate; hence, resistance is not a descriptor of materials which would thrive under low-carbon conditions. We solve for the underlying factors behind these differences and propose a descriptor to optimize Ag reductive displacement in other materials. Further, we show that when evaluated in electrodes with carbon and binder additives all SMOs achieved similar levels of performance, reinforcing the notion that composite electrodes prevent the prediction of structures which would fail in low-carbon electrodes. Our results contribute to understanding where and how Ag^+ should be predistributed in electrodes targeting this mechanism in low-carbon applications and support future testing of carbon-free electrodes as part of battery material evaluation.

Experimental

Syntheses

All chemicals were reagent grade, purchased commercially, and used/stored at ambient conditions without further purification, except for CH_3NH_3Cl which was stored in an N_2 glovebox. The water used in all syntheses, electrolytes and solutions was ultrapure 18 MΩ resistivity.

β-Ag_2MoO_4 (1Mo)

$AgNO_3$ (0.680 g, 4 mmol of Aldrich Lot MKCG5845) dissolved in 15 mL of water was added dropwise to a solution of $Na_2MoO_4\cdot 2H_2O$ (0.484 g, 2.4 mmol of Strem Lot 26713700) dissolved in 15 mL of water. The slight excess of MoO_4^{2-} was utilized to ensure the system maintained an alkaline pH, under which Ag_2MoO_4 is the preferred product. On initial mixture, fine particulates are formed within a cloudy suspension with appearance of milk. Applying ~50 °C heat for 15 minutes, the milk color disappears, and the suspension consists of filterable particulates in clear solution. The phase pure product can be isolated any time after this point. In this study, we performed an overnight reflux, collecting by filtration; 0.50–0.55 g, ~73%. The material can be dried at 100 °C safely; we dried for 1 h.

Monoclinic $Ag_2Mo_2O_7$ (m-2Mo)

Reproduced from Saito *et al.*[41] $AgNO_3$ (0.488 g, 2.9 mmol) dissolved in 20 mL of water was added to 0.226 g (1.6 mmol) of MoO_3 suspended in 20 mL of water. The suspension was refluxed for 5 h, and the resulting solid collected by filtration and washed with water. The material can be dried at 100 °C safely; we dried for 30 minutes. We were unsuccessful at preparing this polymorph by refluxing $AgNO_3$ with ammonium heptamolybdate or acidified MoO_4^{2} due to the presence of triclinic $Ag_2Mo_2O_7$ impurity, which appears in reactions with prolonged temperatures or times; our results agree with other reports.[42,43]

Triclinic $Ag_2Mo_2O_7$ (t-2Mo)

Monoclinic $Ag_2Mo_2O_7$ (200 mg) was heated to 450 °C for 5 h in air in a steel crucible and cooled to room temperature ambiently in 98% yield. The conversion mechanism appears to involve sample melting and subsequent interaction with the container before recrystallizing, as the use of new porcelain crucibles yielded samples with evenly dispersed, 4% Al dopant impurity (which were not studied further). The use of steel eliminates the impurity yet imparts a 2% loss of sample as a tarnish.

© 2021 The Author(s). Published by the Royal Society of Chemistry

Open Access Article. Published on 13 December 2021. Downloaded on 2/20/2026 2:13:40 PM.
This article is licensed under a Creative Commons Attribution 3.0 Unported Licence.

$Ag_2Mo_3O_{10}\cdot 2H_2O$ *via* $(CH_3NH_3)_2Mo_7O_{22}$

We were not successful at isolating this material by refluxing $AgNO_3$ with Mo^{6+} below pH 4, due to the persistence of kinetically favorable **m-2Mo**. We slightly modified the procedure of Dessapt *et al.*[44] to better avoid the appearance of an adventitious hexagonal MoO_3 impurity (see ESI† for details and discussion). Solutions of 1.01 g (15 mmol) of CH_3NH_3Cl in 5 mL of water and 1.21 g of Na_2MoO_4 (6 mmol) in 5 mL of water were mixed and the resultant solution was syringe filtered. 4 M HCl was added dropwise until pH 1.5 was obtained in close correlation with the appearance of a sustained white suspension. The suspension was heated in a Teflon Parr reactor, 120 °C, 6 h. The product white powder $(CH_3NH_3)_2Mo_7O_{22}$ obtained in yield quantitative in Mo was washed with water and acetone. The reader is referred to ESI† for characterization of $(CH_3NH_3)_2Mo_7O_{22}$ and related discussion. Subsequently, $AgNO_3$ (0.235 g) was dissolved in 25 mL of 0.1 M HNO_3, and $(CH_3NH_3)_2Mo_7O_{22}$ (0.300 g) were added. The suspension was refluxed overnight (~16 h) with stirring, and the yellow product was washed with water and ethanol and dried in air.

Electrochemistry materials and methods

All tests were recorded on a Biologic VSP potentiostat. Two electrode cells were constructed inside MTI split cells, with Zn foil anode, 2 M $ZnSO_4$ electrolyte, and Whatman glass fiber filter paper separator. For carbon and binder free working electrodes, silver molybdate powders were pressed between two steel foil sheets at 20 MPa into pre-massed steel gauze (Type 304, 0.001 in wire). Where applicable and mentioned in the text, composite electrodes were prepared using a slurry of silver molybdate : carbon black : PVDF binder prepared in NMP solvent with composition 8 : 1 : 1 by mass and doctor bladed onto steel foil current collector. $\frac{1}{2}''$ circles were punched from this coating and used as electrodes.

Data for galvanostatic intermittent titration technique (GITT) plots were obtained following 360 second pulses at $1e^-$/2 h rates for each material. To maintain a well-defined surface area, working electrodes in these tests were powders pressed evenly onto precut squares of graphene paper. Ionic diffusion coefficients were calculated by:[45]

$$D = \frac{4}{\pi\tau}\left(\frac{nV_m}{S}\right)^2\left(\frac{\Delta E_s}{\Delta E_t}\right)^2$$

Here, τ = pulse length in seconds, n is the moles of material per electrode, V_m is the molar volume for each polymorph (59.7 cm^3 mol^{-1} **1Mo**, 89.6 cm^3 mol^{-1} **m-2Mo**, 88.4 cm^3 mol^{-1} **t-2Mo** and 147 cm^3 mol^{-1} **3Mo**), S is the electrode surface area (in cm^2), ΔE_s is the difference in equilibrated voltage before and after the pulse, and ΔE_t is the difference in voltage between the end of the pulse and the equilibrated potential.

Other materials and methods

PXRD data were recorded on a Rigaku Miniflex with Cu source. SEM data for Fig. 1 were recorded on a JEOL JSM 6610LV,

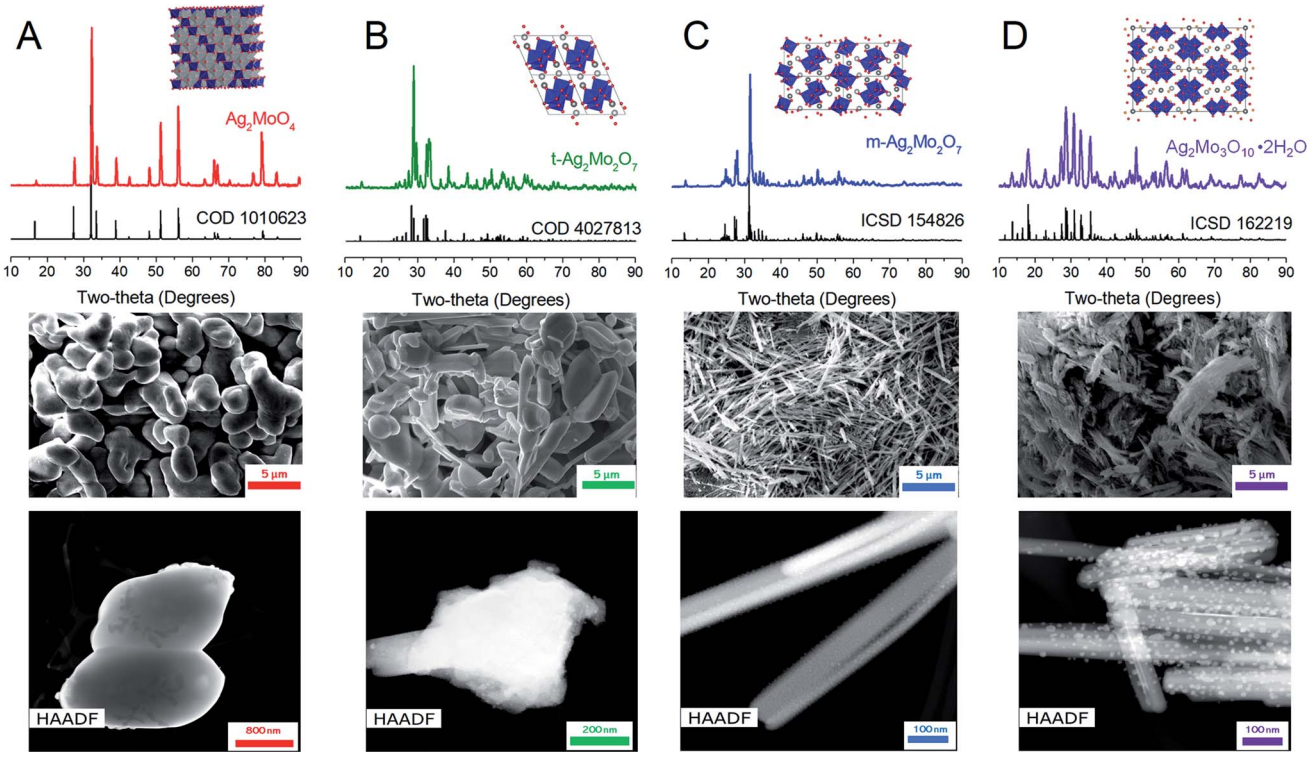

Fig. 1 PXRD, SEM and TEM data for the materials in this work. Experimental powder diffraction patterns (colored traces) are labelled as (A) **1Mo**, (B) **t-2Mo**, (C) **m-2Mo** and (D) **3Mo** over structural references (black traces). In the crystal structure representations blue polyhedra represent Mo and where applicable Ag^+ is represented by two shades of silver, differentiated by symmetry. SEM microscopy images were taken at 5000× magnification.

Open Access Article. Published on 13 December 2021. Downloaded on 2/20/2026 2:13:40 PM.
This article is licensed under a Creative Commons Attribution 3.0 Unported Licence.

whereas data for reduced electrodes were taken with a S-Hitachi-4700-II SEM. Raman data were recorded on a Thermofisher DXR3xi Raman microscope with 532 nm laser excitation. TEM data were recorded on an FEI Talos TEM with an FEI Tecnai F20ST S/TEM. For characterization of reduced electrodes, samples were washed with 0.1 M acetic acid and water following battery disassembly. The freestanding gauze – and if applicable a steel foil support – was inserted directly into SEM and XRD for respective measurements, whereas the sample was scratched from the mesh onto a lacey carbon grid for TEM analysis.

Results

Syntheses and characterization

For this study disilver molybdate (Ag_2MoO_4, **1Mo**) both known polymorphs of disilver dimolybdate ($Ag_2Mo_2O_7$, **2Mo**) and disilver trimolybdate dihydrate ($Ag_2Mo_3O_{10}\cdot 2H_2O$, **3Mo**) were prepared. Literature syntheses were adapted for **1Mo**, **3Mo** and monoclinic **m-2Mo** (see Experimental). For triclinic **t-2Mo**, **m-2Mo** was heated for 5 hours at 450 °C in air; this synthesis improves upon prior reports which have prepared this polymorph *via* solid-state sintering of Ag_2MoO_4 or Ag_2O with MoO_3 requiring 2–4 days.[40,46]

Fig. 1 depicts experimental X-ray diffraction patterns demonstrating phase purity and microscopy characterization of sample morphology. Two of the samples have nanorod morphology (**m-2Mo** and **3Mo**), and the latter exhibits a greater degree of bundling. From the Scherrer equation, the crystallite sizes were 27 and 23 nm respectively. **T-2Mo** and **1Mo** consist of larger particulates; the former with a diverse range from rods to plates, the latter with micron sized, dense potato shapes. These crystallites were 43 and 32 nm, respectively.

High angle annular dark field scanning transmission electron microscopy (HAADF/STEM) images of all samples revealed the existence of surface particles. These were as small as 2 nm in both **2Mo**, 5–15 nm in **3Mo** and, in **1Mo**, the particles were growing as large as 50 nm in real time during the measurement. To our knowledge, all prior studies pursuing transmission electron microscopy characterization on SMOs have reported sample instability and reduction of Ag^+ to Ag^0 in the beam.[41,47–51] EDS spectroscopy confirmed that the surface particles were pure Ag; data for the most prominent samples **1Mo** and **3Mo** are provided as Fig. S1.† Given that no Ag^0 peaks exist in any XRD data, we consider these results consistent with beam damage. For the images in Fig. 1, EDS verified the compositional Ag : Mo ratios expected for each sample (Fig. S2†) and SEM/EDS mapping confirmed the elements were evenly distributed on the micron scale (Fig. S3†). One rationale for the beam damage results could be the Ag^+–Ag^+ distances of each SMO, when compared to the product Ag^0 crystals containing atoms 2.89 Å apart. The **2Mo** samples which exhibited very small Ag^0 particles do not have Ag^+–Ag^+ distances shorter than 3.36 Å. By contrast, **3Mo** contains one of the shortest Ag^+–Ag^+ distances of any SMO in this study (3.17 Å), and in **1Mo** all Ag^+–Ag^+ distances are 3.27 Å. Hence, Ag^0 appears to grow more prominently in the TEM beam when the ions do not have to migrate as far.

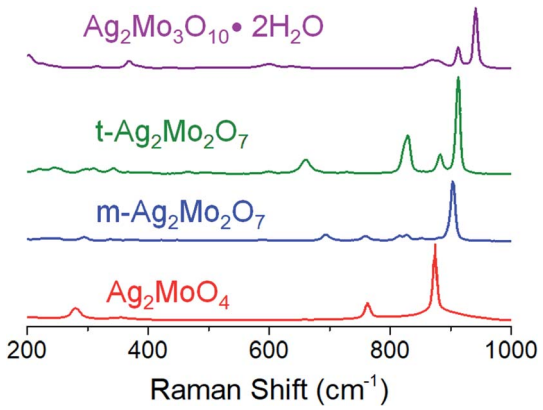

Fig. 2 Raman spectra of the materials in this study; see text for peak values.

Fig. 2 depicts Raman spectroscopy characterization ($\lambda = 532$ nm). **1Mo** exhibits peaks at 873, 762, 354 and 279 cm^{-1}, which are in agreement within ± 1 cm^{-1} to the known A_{1g}, $2T_{2g}$ and E_g stretches respectively.[52,53] **m-2Mo** has a major peak at 905 cm^{-1} with minor bands at 853, 828, 817, 760 and 694 cm^{-1}, which are in agreement within ± 2 cm^{-1} to other data.[43] We are not aware of other Raman spectroscopy data for **t-2Mo**, which our results find a major peak at 913 cm^{-1} with minor bands at 864, 830, 662, 344 and 311 cm^{-1}. Finally, **3Mo** gives a major peak at 941 cm^{-1} with minor bands at 912, 869, 636, 598, 368, 314 and 202 cm^{-1}, which agrees with literature.[44] Of particular emphasis from this dataset: larger values for the major peak at *ca.* 900 cm^{-1} indicate stronger Mo–O bonds,[54] and by extension more acidic oxos. Our Raman data therefore confirms the expected trend MoO_4^{2-} < $Mo_2O_7^{2-}$ < $Mo_3O_{10}^{2-}$ for increasing acidity of the molybdate frameworks.[43,55]

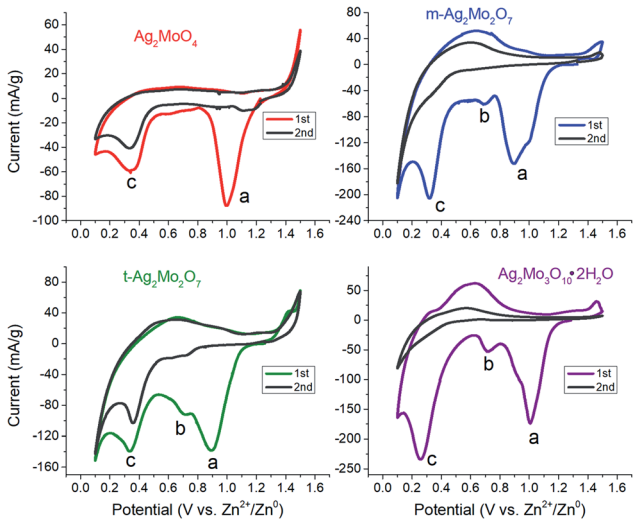

Fig. 3 Cyclic voltammetry at 0.1 mV s^{-1} for each of the materials in this study. Conditions: 2 M $ZnSO_4$ electrolyte, Zn foil anode and reference.

© 2021 The Author(s). Published by the Royal Society of Chemistry

Open Access Article. Published on 13 December 2021. Downloaded on 2/20/2026 2:13:40 PM.
This article is licensed under a Creative Commons Attribution 3.0 Unported Licence.

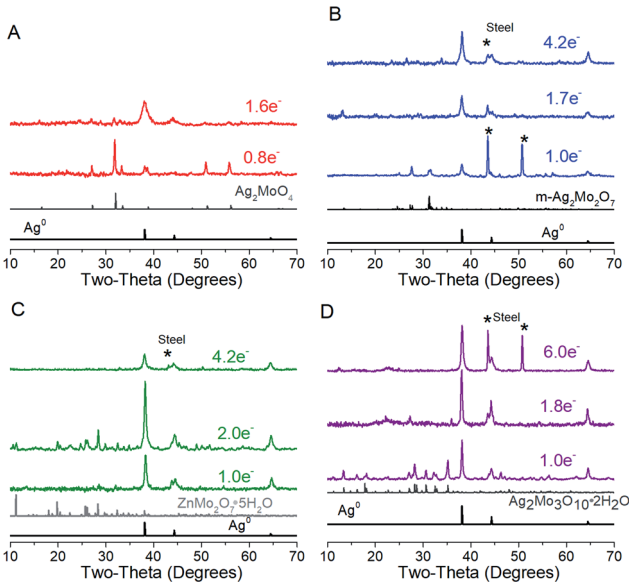

Fig. 4 XRD characterization of electrodes reduced at 5 mA g^{-1}; data are also representative up to 40 mA g^{-1}. (A) Ag_2MoO_4, (B) m-$Ag_2Mo_2O_7$, (C) t-$Ag_2Mo_2O_7$, and (D) $Ag_2Mo_3O_{10}\cdot 2H_2O$.

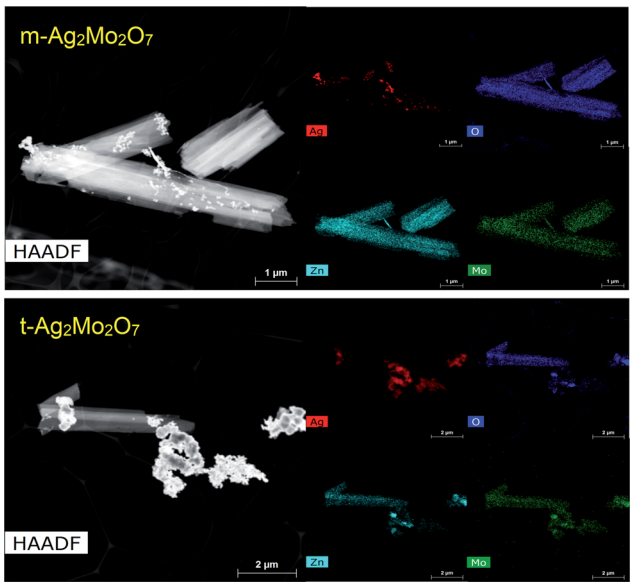

Fig. 5 HAADF/STEM and EDS maps for **m-2Mo** (top) and **t-2Mo** (bottom) samples reduced by 2ee at $1e^-$/2 h, showing Zn displacing Ag from the initial structures.

Electrochemistry mechanism: reduction of Ag^+

Cyclic voltammograms of SMO powders as cathodes in 2-electrode AZIBs are provided as Fig. 3. All SMO's exhibit a cathodic peak 'a' located at 0.90 (**2Mo**) through 1.00 V (**1Mo**, **3Mo**), which is assigned to the reduction of Ag^+ based on several lines of evidence. (1) It is the most plausible thermodynamic match based on reduction potentials measured of Ag^+ and Mo^{6+} standards (Fig. S4†), which occurred across 1.0–1.2 V and 0.20–0.38 V ranges *vs.* Zn^{2+}/Zn^0 respectively. (2) In all SMO's no more than 2 electron equivalents (ee) of charge per mole can be passed at peak 'a'; this precisely matches the amount of charge needed to reduce both formula silvers quantitatively. (3) XRD (Fig. 4) identifies Ag^0 in samples reduced by 0.8–1.0ee at the peak 'a' potential. (4) The Scherrer equation, when applied to the main peak at 38° 2θ, calculates the Ag^0 crystallite size as increasing up to 2ee, beyond which there is no significant difference (Fig. S5†). This is consistent with the Ag^0 network growing in this region to form crystals that ultimately exhibited a correlation of increasing size with decreasing $[Ag^+]_0$, with 6 nm in **1Mo**, 17 nm for **m-2Mo**, 18 nm for **t-2Mo** and 28 nm for **3Mo**. (5) Impedance data (discussed later) shows all SMO electrodes become ~100× more conductive within 0.05ee, consistent with an expected result from forming Ag^0 *in situ*.

The peak current in CV's is known to be the combination of surface capacitive effects – which are proportional to scan rate ν – and bulk diffusion effects – which are proportional to $\nu^{1/2}$. Hence, for the overall dependence of current on scan rate *via* the equation:[56]

$$i = a\nu^b \quad (1)$$

A plot of $\log(i)$ *vs.* $\log(\nu)$ should yield a line with slope b between 0.5 (pure diffusion) and 1 (pure capacitance). Applied to peak 'a', the b values measured for the **2Mo** and **1Mo** samples (0.55–0.67, Fig. S6†) were all internally consistent with evidence of Ag^+ reduction limited by diffusion in the bulk. However, the b value for **3Mo** (0.88) instead suggests a more surface-limited, pseudocapacitive mechanism. In support of these electrochemistry assignments, XRD identified $ZnMo_2O_7\cdot 5H_2O$ (ICSD 245617) as the other crystalline product after 2ee reduction of **t-2Mo** (Fig. 4C), thereby proving a full bulk reductive displacement mechanism occurring *via*:

$$Ag_2Mo_2O_7 + Zn^{2+} + 2e^- + 5H_2O \rightarrow 2Ag + ZnMo_2O_7\cdot 5H_2O \quad (2)$$

The $ZnMo_2O_7\cdot 5H_2O$ is less crystalline than the starting **t-2Mo** (25 *vs.* 43 nm, respectively). Attempts to detect a $ZnMo_2O_7$ phase from reduction of less-crystalline **m-2Mo** were unsuccessful but HAADF/STEM characterization (Fig. 5) provides evidence further confirming a closely related mechanism. In these images both 2ee reduced **2Mo** samples were found to contain particles analyzing as pure Ag in addition to sheets clearly characterized by EDS as the zinc-molybdenum oxide

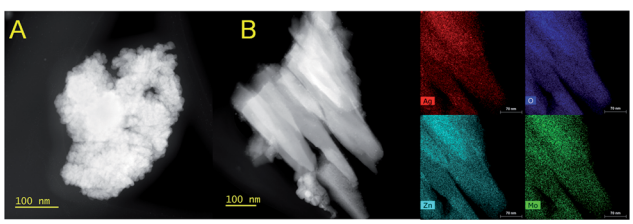

Fig. 6 HAADF/STEM and EDS maps for **1Mo** reduced by 1.6ee at $1e^-$/2 h. (A) The morphology of a pure Ag aggregate. (B) Sheets of $ZnMoO_x$ with residual silver existing as ultrafine particles; the yellow box was analyzed by EDS.

Open Access Article. Published on 13 December 2021. Downloaded on 2/20/2026 2:13:40 PM. This article is licensed under a Creative Commons Attribution 3.0 Unported Licence.

(Fig. 5, S7 and S8†). SEM-EDS mapping on the micron scale (Fig. S9†), further confirms the primarily bulk mechanism for **m-2Mo**.

Reduced **1Mo** electrodes consisted of two types of particles: aggregates of pure nanosized Ag (Fig. 6A), and larger sheets with Ag : Zn : Mo of 1 : 2 : 2 (Fig. 6B). The sheets were covered in ultrafine, ~2 nm particles resembling the Ag in the aggregates (Fig. S10†), though EDS mapping does not assign the total Ag concentration detected to solely those particles. The close spatial association of Zn with Mo, combined with clear evidence of Ag separate from Mo seen also by SEM (Fig. S11†), is also consistent with a bulk reduction displacement mechanism of:

$$Ag_2MoO_4 + Zn^{2+} + 2e^- \rightarrow 2Ag + ZnMoO_4 \quad (3)$$

We repeatedly detected Ag^0 as the only crystalline product from reduction of **3Mo**. Microscopy images of reduced **3Mo** electrodes are shown in Fig. 7 and S12† and were consistent with the absence of a bulk mechanism by electrochemistry. In this data, the major samples detected were sheets with high concentrations of Zn + O, with Mo existing in low concentrations and in distributions not matching Zn. The Zn + O sheets were either in direct contact or closely associated with large domains of Ag, which confirmed the XRD data detecting increased Ag^0 crystallinity. These results overall do not provide evidence for substitution of Zn into the $Mo_3O_{10}^{2-}$ framework. Rather, the data suggests the existence of a silver-coated basic zinc salt (*e.g.*, $Zn_4SO_4(OH)_6$), which is a known product from Zn/MoO_3 and numerous other Zn electrochemistries[57] as resulting from a mechanism in which the pH of the electrolyte increases. We had some success detecting a pH increase in $ZnCl_2$ electrolyte, which allowed the identification of simonkoellite $Zn_5(OH)_8Cl_2\ H_2O$ on the anode (Fig. S13†) by PXRD.

The close association of Ag^0 with the basic zinc salt observed both by TEM and SEM (Fig. S14†) suggests a **3Mo** reduction mechanism which increases the electrolyte's pH locally near where Ag^0 forms. Here, we propose:

$$Ag_2Mo_3O_{10}\cdot 2H_2O + 2e^- \rightarrow 2Ag + 3MoO_3 + H_2O + 2OH^- \quad (4)$$

$$Zn^{2+} + xSO_4^{2-} + (2 - 2x)OH^- \rightarrow Zn(SO_4)_x(OH)_{2-2x} \quad (5)$$

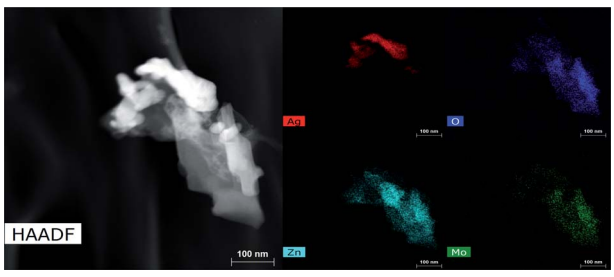

Fig. 7 HAADF/STEM and EDS maps for **3Mo** reduced by 2ee at 1e⁻/2 h, showing regions of Zn + O mixed with Ag. The Zn : Mo ratio is 2.3 : 1.

Electrochemistry mechanism, subsequent steps

We observed two reduction steps: a minor one at 0.7 V and a major one at ~0.3 V (labeled as (b) and (c) respectively) in CV's of both **2Mo** and **3Mo** following the consumption of their Ag^+ ions (Fig. 3).

Given that aqueous Mo^{6+} standards reduce at 0.3 V (Fig. S4†), and that peak 'b' cannot account for quantitative reduction of Mo^{6+} in any sample, peak 'c' is assigned to the reduction of Mo^{6+}.

The assignment of peak 'b' occurring for a fraction of the Mo^{6+} is developed by considering that it is most prominent in **t-2Mo** and absent from the CV of **1Mo**. The only redox-active component in the **t-2Mo** electrode capable of accounting for peak 'b' is $ZnMo_2O_7\cdot 5H_2O$, which is a layered structure of $Mo_2O_7^{2-}$ chains linked by Zn^{2+} cations.[58] Other layered MoO_3 AZIB cathodes are well-known to exhibit peaks at 0.7 V and ~0.3 V.[57,59] By contrast, the proposed stoichiometry of the phase in the **1Mo** sample is $ZnMoO_4$, for which all known crystalline polymorphs[60,61] are not layered. Therefore, peak 'b' is proposed to indicate the existence of layered domains in the Mo^{6+} oxide produced following reduction of each sample's silver ions.

Prior literature has shown the duration of each potential step at 0.7 V and 0.3 V for layered Mo^{6+} cathodes is ascribed to the increasing effects of H_3O^+ rather than Zn^{2+} as the charge carrier.[57,59] We utilized the galvanostatic intermittent titration technique (GITT) to characterize peaks 'b'–'c' since Zn^{2+} diffusion into MoO_3 (10^{-10} to 10^{-12} $cm^2\ s^{-1}$)[59,62] is known to be slower than H^+ (10^{-8} to 10^{-9} $cm^2\ s^{-1}$).[59] For all SMO's, we measured ion diffusion coefficients within the range of 10^{-11} to 10^{-12} $cm^2\ s^{-1}$ while on the Ag^+ reduction plateau, which is where either Zn diffusion or growth is confirmed by microscopy (Fig. S15†). In direct correlation with the drop to lower potentials for peaks 'b'–'c', the ionic diffusion coefficients increased by *ca.* 2 orders of magnitude. Therefore, Zn^{2+} clearly charge balances the reduction of $2Ag^+$ and, once complete, H^+ is proposed to charge balance the reduction of the resulting $ZnMoO_x$ or MoO_x.

Under our conditions the SMO's exhibited poor cyclability by CV (Fig. 3) and most other methods tested by our group. Both **2Mo** and **3Mo** show an anodic curve at 0.6 V, assigned to the reoxidation of a fraction of the reduced Mo, which is also observed for aqueous Mo^{6+} standards. In all SMO's the anodic peak for Ag^0 initiates at 1.5 V but to prevent a significant loss of the electronic conductive network we bounded CVs at that potential. Subsequent scans showed no appreciable current for the reduction of Ag^+. Our findings are largely in agreement with the consensus that MoO_3 in aqueous batteries exhibits poor capacity retention upon cycling,[63] with evidence so far suggesting that this is due to the dissolution of reduced Mo which is known from aqueous electrochemistry of Mo oxide passive layers.[64] Numerous reports have indicated generally underwhelming metrics for aqueous MoO_3 battery or capacitor electrochemistry unless polypyrrole composites, gel electrolytes, or water-in-salt electrolytes are utilized to stop dissolution;[57,63,65–69] these strategies lie outside the scope of this study.

© 2021 The Author(s). Published by the Royal Society of Chemistry

Open Access Article. Published on 13 December 2021. Downloaded on 2/20/2026 2:13:40 PM.
This article is licensed under a Creative Commons Attribution 3.0 Unported Licence.

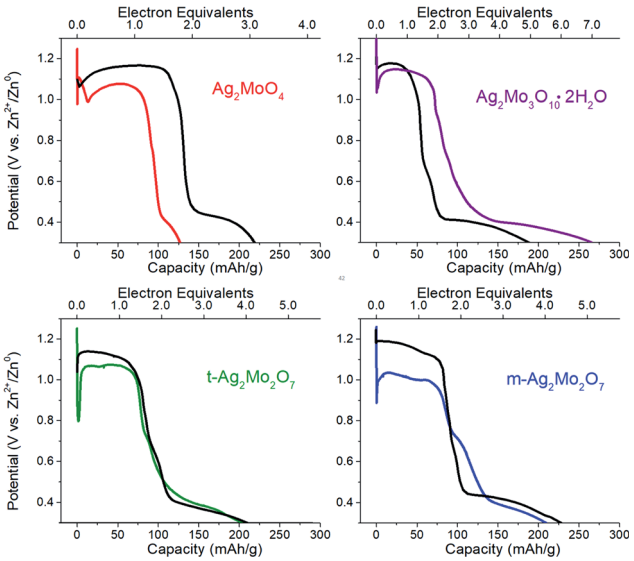

Fig. 8 Representative galvanostatic discharge at 40 mA g^{-1} rates for the materials in this study. Working electrodes are the pure powder pressed into steel mesh (colored traces: red **1Mo**, green **t-2Mo**, blue **m-2Mo** and purple **3Mo**) or a composite electrode with 80/10/10 active material/carbon/PVDF composition (black traces). Conditions: 2 M $ZnSO_4$ electrolyte, Zn foil anode and reference.

Metrics for Ag^+ reduction

We compared the electrochemical performance of SMO's as stand-alone pellets (Fig. 8, colored traces) *vs.* composite electrodes containing carbon predistributed (Fig. 8, black traces) at 40 mA g^{-1} rates. Notably, the stand-alone pellets all exhibit an initial voltage drop followed by a recovery – a property well known in SVO cathodes and analogs[31,70,71] as the initial polarization being overcome by the *in situ* generation of a conductivity change provided by the Ag^0 network. We consider the following metrics:

(1) Operating voltage plateau. With a carbon network able to lower interparticle resistance, the initial voltage drop/recovery is mitigated in all cases. The resulting reduction of silver is sustained at 1.17 ± 0.02 V, crucially irrespective of the SMO structure. However, without carbon only **3Mo** is capable of attaining >1.1 V for the duration of the plateau; by contrast, **1Mo** and both **2Mo** are least 50 mV lower.

(2) Capacity at high voltage. For all SMO's with carbon the $2e^-$ reduction level occurs as the voltage falls from the 1.17 V plateau. While both **2Mo** and **3Mo** reach this boundary without carbon, **1Mo** does not discharge by $2e^-$ without carbon.

(3) Capacity at low voltage. With Mo^{4+} as the lowest oxidation state known in Zn/MoO_3 batteries, plausible upper bound capacities are 4 electrons in **1Mo** (284 mA h g^{-1}), 6 electrons in **2Mo** (312 mA h g^{-1}) and 8 electrons in **3Mo** (304 mA h g^{-1}). Experimentally, we measured **3Mo** (89%, 270 mA h g^{-1}) > **m-2Mo** (67%, 210 mA h g^{-1}) ≈ **t-2Mo** (65%, 200 mA h g^{-1}) ≫ **1Mo** (45%, 130 mA h g^{-1}) when ranking the percentage delivered by carbon-free electrodes above 0.3 V. **3Mo** significantly underperforms in the composite electrode suggesting the binder is inhibiting this material's more pseudocapacitive mechanism.

For greater resolution on the formation of the Ag^0 network in stand-alone pellets pulse tests were performed, where 10 × 0.05 electron equivalent intervals were titrated into each SMO; electrodes were relaxed to a stable OCV between pulses. Fig. 9A depicts representative Nyquist plots of SMO electrodes prior to

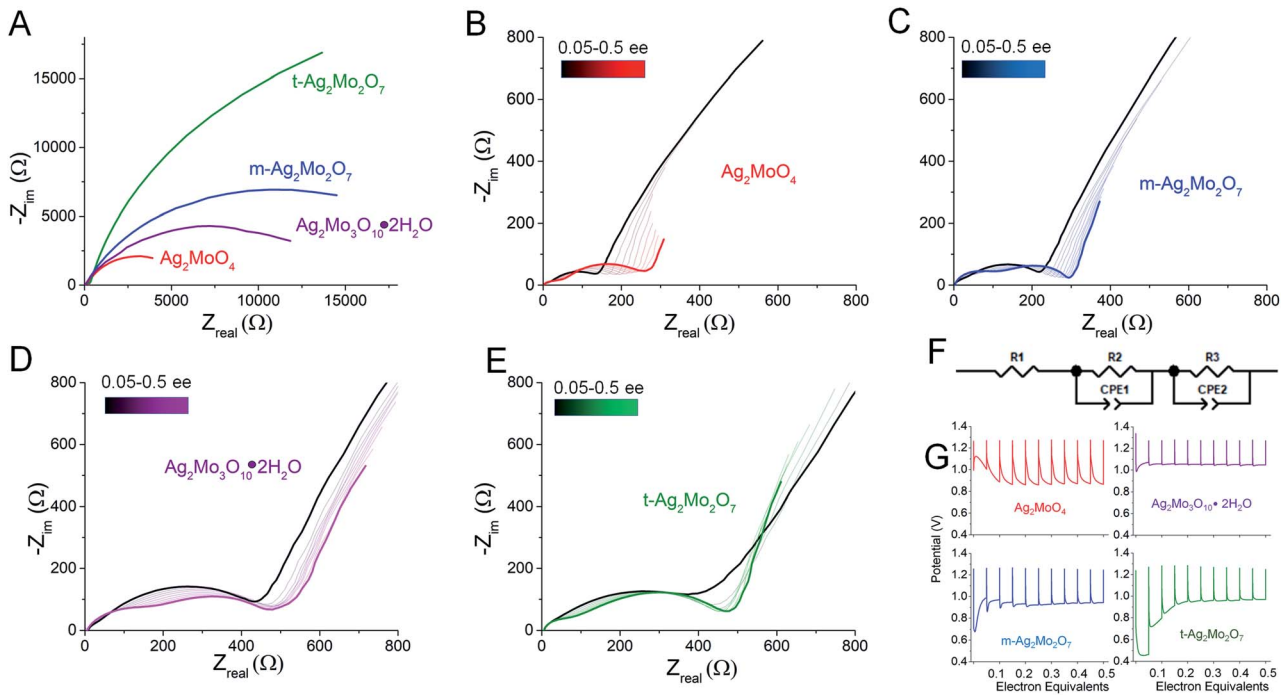

Fig. 9 (A) Representative Nyquist plots of pellet electrodes; (B–E) Nyquist plots following titration of 0.05 electron equivalents into each SMO at 40 mA g^{-1}; (F) the circuit used to fit the two semicircles in the impedance data. (G) Potential *vs.* electron equivalents at 40 mA g^{-1} rates.

© 2021 The Author(s). Published by the Royal Society of Chemistry

Open Access Article. Published on 13 December 2021. Downloaded on 2/20/2026 2:13:40 PM.
This article is licensed under a Creative Commons Attribution 3.0 Unported Licence.

any reduction. For quantitative fit, the semicircles were modeled *via* a Randles-type circuit with two R/C parallels, (Fig. 9F), which has been used for other silver metal oxides.[1,3,31,72] In this circuit, R_1 is the solution resistance, the R_2/CPE parallel models the anode and the R_3/CPE parallel models the cathode. R_3 is of interest as it represents the interparticle charge transfer resistance, R_{ct}. Results from fittings quantify the initial R_{ct} ranging 9–45 kΩ.

The electrode potentials were monitored during each 0.05 electron pulse (Fig. 9G). Fig. 9B–E depict that, upon relaxation after the first 0.05 electron equivalent reduction, all SMO's exhibit a compressed semicircle indicative of a decreased charge transfer resistance. R_{ct} is lower than 530 Ω in all cases, representing a resistance decrease of up to 100×, with the largest decrease from the **t-2Mo** electrode.

The first 0.05ee is sufficient to generate enough Ag^0 to recover the voltage in **1Mo**, **3Mo** and **m-2Mo** before the end of pulse duration (Fig. 9G). That **t-2Mo** requires additional Ag^0 is not ascribed to its morphology but rather its initially highest R_{ct}, which causes a higher polarization to need to overcome. The data in Fig. 9G clearly show that the initial voltage drop of the electrode is proportional to the initial resistance; we observed similar trends in galvanostatic reduction (Fig. S16†).

In comparison to the 0–0.05ee decrease, subsequent titration of 0.05–0.5ee changed R_{ct} far less significantly. In particulate samples R_{ct} gets slightly worse: **1Mo** increased from 141 to 275 Ω (Fig. 9B), correlating with an electrode which operated at 0.87–0.90 V in each pulse. For **t-2Mo** (Fig. 9E) the increase observed was 390–465 Ω, but this primarily occurred in early electron increments and ultimately correlated with higher pulse voltages of 0.97 V. **m-2Mo** mostly retained the same R_{ct} (230–220 Ω, Fig. 9C) and exhibited a comparable 0.94 V pulse voltage (Fig. 9G). Finally, **3Mo** recovered voltage to the highest plateau at 1.05 V, but this correlated with a relatively high R_{ct} that was consistently improving with each pulse from 528 to 385 Ω (Fig. 9D).

Collectively our results show there is no association of low R_{ct} with operational pulse voltage, which varies for Ag^+ reduction by as much as 140 mV. The clear potential order **1Mo** < **2Mo** < **3Mo** from pulse tests matches that from galvanostatic reduction (point 1). Given that each SMO appears to form a sufficient Ag^0 network to fully recover voltage within 0.2ee, we evaluated the silver networks by two more metrics:

(4) Rate capability. We reduced each carbon-free SMO by 0.2 electrons at $0.5e^-\ h^{-1}$ rates to form a Ag^0 network. Then, the reduction rate was increased by a factor of 5. Over the next 1.5 electrons – the upper bound for comparison – the resulting electrodes all deliver a fraction of the W h kg^{-1} energy relative to when the rate is unmodified. For the sample data shown in Fig. 10, top, this fraction was 84% (**3Mo**) > 73% (**t-2Mo**) > 48% (**m-2Mo**) > 15% (**1Mo**).

(5) Formation rate kinetics of Ag^0. We initiated reduction of each carbon-free SMO at $3e^-\ h^{-1}$; a 6× faster rate than the prior test (Fig. 10, bottom). **T-2Mo**, which needs more Ag^0 to overcome an intrinisically higher R_{ct}, fails this test most prominently. At the other extreme, **3Mo** delivered 200 mA h g^{-1}, which is 86% of the value from the 6× slower rate.

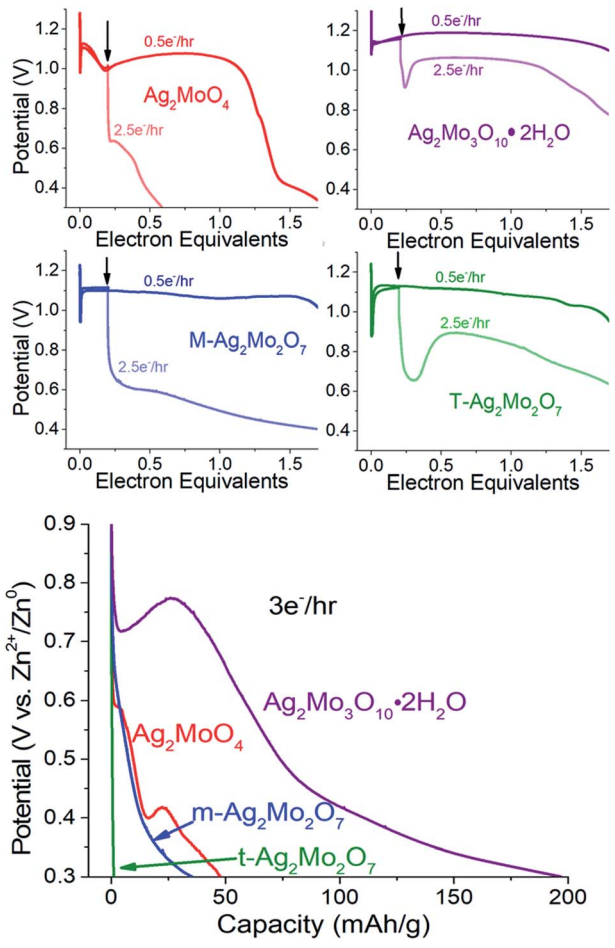

Fig. 10 Top: The SMOs are discharged at $0.5e^-\ h^{-1}$ rates until the position of the arrow at 0.2ee. Light curves indicate a rate change to $2.5e^-\ h^{-1}$ while the dark curve indicates the remainder of discharge at $0.5e^-h^{-1}$. Bottom: Representative galvanostatic discharge at $3e^-\ h^{-1}$ for the materials in this study.

Discussion

In the design of cathodes capable of displacing Zn^{2+} for $2Ag^+$ in aqueous conditions, the above data (points 1–5) suggests a trend of **1Mo** ≪ **m-2Mo** ≤ **t-2Mo** for the most optimized initial structure and the "best" Ag^0 network at replicating carbon composites. However, much superior metrics are obtained by **3Mo**, which does not perform $Zn^{2+}/2Ag^+$ bulk substitution directly nor yields electrodes with lowest R_{ct}. Such a trend is not addressed by morphology nor crystallinity because both are comparable to the worse-performing **m-2Mo**. Rather, the trend appears easily explained in the context of the acidity of the molybdate framework by Raman spectroscopy (Fig. 2). The consequence of a molybdate framework with greater acidity is that the Ag^+ in **3Mo** have longer Ag–O bonds 2.44–2.88 Å relative to **m-2Mo** (2.33–2.64 Å), **t-2Mo** (2.27–2.76 Å), and especially **1Mo** (2.31 Å). With the Ag^+ ions most weakly bound to oxygen, the energy penalty for Ag–O bond breakage is lowered and results in

© 2021 The Author(s). Published by the Royal Society of Chemistry

Open Access Article. Published on 13 December 2021. Downloaded on 2/20/2026 2:13:40 PM.
This article is licensed under a Creative Commons Attribution 3.0 Unported Licence.

improved access to Ag^+ with minimal voltage loss and fast kinetics.

The tradeoff that naturally follows by making a cation easier to displace from a framework is that it becomes harder to put a new cation in. As our measurements show, this tradeoff in molybdates is at first surmountable (because **2Mo** > **1Mo**) but then is avoided entirely through a charge balancing mechanism switch (**3Mo**). Hence, our results appear to demonstrate the existence of a "crossover" acidity below which Ag^+ can be made more accessible and above which Zn^{2+} insertion no longer occurs. In AZIBs this crossover thus occurs between the acidities of $Mo_2O_7^{2-}$ and $Mo_3O_{10}^{2-}$ frameworks. As molecular species, it is intriguing that 10 mM solutions give pH's of 4.58 and 3.52 respectively[55] which appear to straddle the typical ~4.0–4.5 pH of aqueous $ZnSO_4$.

Prior reports on nonaqueous Li/SVO cells do not appear to mention this concept, though there are striking comparisons. Several reports qualitatively correlated materials with higher Ag^+ content promoting overall higher voltage but with a tradeoff of lower capacity.[24,73,74] This correlation doesn't describe structures, but our Zn/SMO composite electrode results agree with the conceptual trend. Chen *et al.* proposed silver ions in SVO interlayers were more facile to reduce than silver ions as structured octahedra.[75] In our study the silver ions in both **2Mo** and **3Mo** qualify as "interchain", compared to the structurally rigid Ag^+ in **1Mo**, but with an observed order of **1Mo** < **2Mo** < **3Mo**, we note this description appears conceptually correct but incomplete. Therefore, our results not only appear consistent with prior trends in nonaqueous electrochemistry but also provide an overall revision.

Our data do not rule out the solvation of Ag^+ with water molecules unique to **3Mo** as another possible descriptor causing or aiding a change in mechanism. However, a kinetic advantage to weakly-bound Ag^+ sites has been noted in nonaqueous chemistry recently: purposeful placement of Ag^+ on the surface of $Ag_xMn_8O_{16}$ nanowires improves fast-rate discharge capacity by 2-fold compared to when the Ag^+ was added to the bulk MnO_x tunnel structure.[28,72] We propose, therefore, that this design principle has applications beyond aqueous electrolyte and Zn^{2+} ions.

Conclusions

This investigation was motivated by needs to understand reduction displacement mechanisms under aqueous conditions and to establish the impacts of varying the initial distribution, concentration, and structure of Ag^+ in mixed metal oxides. We have found across a systematic electrochemical study of four silver molybdates that less than 0.2 electron equivalents (10% of Ag^+) need be reduced to reach locally low values of R_{ct} in all cases, and while these values are ultimately comparable in magnitude irrespective of initial structure, they are not predictive of materials which are robust to rate changes nor those which can minimize losses when reducing the carbon content of electrodes. The best descriptor for this is the increase of acidity of molybdate frameworks, which first causes improved displacement of Ag^+ for Zn^{2+} in aqueous electrolyte before forcing an alternative pseudocapacitive mechanism of charge balance to predominate. This factor contributed more than differences in crystallinity or morphology across the samples.

All these materials and mechanisms deliver comparable voltage for the Ag^+ reduction when utilized in composite electrodes containing carbon and binder, but at least one case exists (**3Mo**) where additives are in fact detrimental to the mechanism. So, while composite electrodes are necessary to advance the electrochemistry of new Zn^{2+} hosts and attain good individual metrics, we have shown here that they potentially can improve the performance of materials with fundamental weaknesses that only research in efforts to increase functional percentages in the next generation of electrochemical energy storage devices will expose.

Conflicts of interest

There are no conflicts to declare.

Acknowledgements

This work was supported by Valparaiso University (B. G.), the Indiana Academy of Science (J. P. Z.), and the NSF EPIC program #1564855 (A. H.). Use of the Center for Nanoscale Materials, an Office of Science user facility, was supported by the U.S. Department of Energy, Office of Science, Office of Basic Energy Sciences, under Contract No. DE-AC02-06CH11357. We thank the Chicago State University Core Microscopy Facility and Andrew Maselli for SEM access. We thank Rachel Koritala for SEM training, Jianguo Wen for TEM training, and Altug Poyraz for helpful discussions.

References

1 D. C. Bock, A. M. Bruck, C. J. Pelliccione, Y. Zhang, K. J. Takeuchi, A. C. Marschilok and E. S. Takeuchi, *RSC Adv.*, 2016, **6**, 106887–106898.
2 K. W. Knehr and A. C. West, *J. Electrochem. Soc.*, 2016, **163**, A1576–A1583.
3 K. C. Kirshenbaum, D. C. Bock, Z. Zhong, A. C. Marschilok, K. J. Takeuchi and E. S. Takeuchi, *Phys. Chem. Chem. Phys.*, 2014, **16**, 9138–9147.
4 K. Kirshenbaum, D. C. Bock, C.-Y. C.-Y. Lee, Z. Zhong, K. J. Takeuchi, A. C. Marschilok and E. S. Takeuchi, *Science*, 2015, **347**, 149–154.
5 K. C. Kirshenbaum, D. C. Bock, A. B. Brady, A. C. Marschilok, K. J. Takeuchi and E. S. Takeuchi, *Phys. Chem. Chem. Phys.*, 2015, **17**, 11204–11210.
6 D. C. Bock, A. C. Marschilok, K. J. Takeuchi and E. S. Takeuchi, *Electrochim. Acta*, 2012, **84**, 155–164.
7 D. Kundu, B. D. Adams, V. Duffort, S. H. Vajargah and L. F. Nazar, *Nat. Energy*, 2016, **1**, 16119.
8 A. Konarov, N. Voronina, J. H. Jo, Z. Bakenov, Y.-K. Sun and S.-T. Myung, *ACS Energy Lett.*, 2018, **3**, 2620–2640.
9 H. Li, L. Ma, C. Han, Z. Wang, Z. Liu, Z. Tang and C. Zhi, *Nano Energy*, 2019, **62**, 550–587.

© 2021 The Author(s). Published by the Royal Society of Chemistry

Open Access Article. Published on 13 December 2021. Downloaded on 2/20/2026 2:13:40 PM. This article is licensed under a Creative Commons Attribution 3.0 Unported Licence.

10 B. Lan, Z. Peng, L. Chen, C. Tang, S. Dong, C. Chen, M. Zhou, C. Chen, Q. An and P. Luo, *J. Alloys Compd.*, 2019, **787**, 9–16.
11 L. Shan, Y. Yang, W. Zhang, H. Chen, G. Fang, J. Zhou and S. Liang, *Energy Storage Mater.*, 2019, **18**, 10–14.
12 S. Guo, G. Fang, S. Liang, M. Chen, X. Wu and J. Zhou, *Acta Mater.*, 2019, **180**, 51–59.
13 Q. Li, Y. Liu, K. Ma, G. Yang and C. Wang, *Small Methods*, 2019, **3**, 1900637.
14 J. Zeng, K. Chao, W. Wang, X. Wei, C. Liu, H. Peng, Z. Zhang, X. Guo and G. Li, *Inorg. Chem. Front.*, 2019, **6**, 2339–2348.
15 H. Liu, J. Wang, H. Sun, Y. Li, J. Yang, C. Wei and F. Kang, *J. Colloid Interface Sci.*, 2020, **560**, 659–666.
16 Y. Liu, Q. Li, K. Ma, G. Yang and C. Wang, *ACS Nano*, 2019, **13**, 12081–12089.
17 X. Yu, F. Hu, F. Cui, J. Zhao, C. Guan and K. Zhu, *Dalton Trans.*, 2020, **49**, 1048–1055.
18 X. Yu, F. Hu, Z.-Q. Q. Guo, L. Liu, G.-H. H. Song and K. Zhu, *Rare Met.*, 2021, DOI: 10.1007/s12598-021-01771-8.
19 Y. Yang, Y. Tang, S. Liang, Z. Wu, G. Fang, X. Cao, C. Wang, T. Lin, A. Pan and J. Zhou, *Nano Energy*, 2019, **61**, 617–625.
20 M. S. Chae, R. Attias, B. Dlugatch, Y. Gofer and D. Aurbach, *ACS Appl. Energy Mater.*, 2021, **4**, 10197–10202.
21 L. Shan, J. Zhou, M. Han, G. Fang, X. Cao, X. Wu and S. Liang, *J. Mater. Chem. A*, 2019, **7**, 7355–7359.
22 L. Chen, Z. Yang, J. Wu, H. Chen and J. Meng, *Electrochim. Acta*, 2020, **330**, 135347.
23 Y. Zhang, A. Chen and J. Sun, *J. Energy Chem.*, 2021, **54**, 655–667.
24 K. J. Takeuchi, A. C. Marschilok, S. M. Davis, R. A. Leising and E. S. Takeuchi, *Coord. Chem. Rev.*, 2001, **221**, 283–310.
25 G. Belardi, P. Ballirano, M. Ferrini, R. Lavecchia, F. Medici, L. Piga and A. Scoppettuolo, *Thermochim. Acta*, 2011, **526**, 169–177.
26 A. Accardo, G. Dotelli, M. L. Musa and E. Spessa, *Appl. Sci.*, 2021, **11**, 1–32.
27 L. Li, E. Fan, Y. Guan, X. Zhang, Q. Xue, L. Wei, F. Wu and R. Chen, *ACS Sustainable Chem. Eng.*, 2017, **5**, 5224–5233.
28 P. F. Smith, A. B. Brady, S. Y. Lee, A. M. Bruck, E. Dooryhee, L. Wu, Y. Zhu, K. J. Takeuchi, E. S. Takeuchi and A. C. Marschilok, *ACS Appl. Mater. Interfaces*, 2018, **10**, 400–407.
29 J. Huang, X. Hu, A. B. Brady, L. Wu, Y. Zhu, E. S. Takeuchi, A. C. Marschilok and K. J. Takeuchi, *Chem. Mater.*, 2018, **30**, 366–375.
30 K. C. Kirshenbaum, D. C. Bock, C.-Y. Lee, Z. Zhong, K. J. Takeuchi, A. C. Marschilok and E. S. Takeuchi, *Science*, 2015, **347**, 149–154.
31 M. M. Huie, D. C. Bock, Z. Zhong, A. M. Bruck, J. Yin, E. S. Takeuchi, K. J. Takeuchi and A. C. Marschilok, *J. Electrochem. Soc.*, 2017, **164**, A6007–A6016.
32 J. Huang, A. S. Poyraz, S.-Y. Lee, L. Wu, Y. Zhu, A. C. Marschilok, K. J. Takeuchi and E. S. Takeuchi, *ACS Appl. Mater. Interfaces*, 2017, **9**, 4333–4342.
33 L. Wang, Q. Wu, A. Abraham, P. J. West, L. M. Housel, G. Singh, N. Sadique, C. D. Quilty, D. Wu, E. S. Takeuchi, A. C. Marschilok and K. J. Takeuchi, *J. Electrochem. Soc.*, 2019, **166**, A3575–A3584.
34 B. Gatehouse and P. Leverett, *Chem. Commun.*, 1969, 1093–1094.
35 R. W. G. Wyckoff, *J. Am. Chem. Soc.*, 1922, **44**, 1994–1998.
36 W. Lasocha, J. Jansen and H. Schenk, *J. Solid State Chem.*, 1994, **109**, 1–4.
37 F. Bonino, M. Lazzari and B. Scrosati, *J. Electroanal. Chem.*, 1978, **93**, 117–125.
38 V. Kumar, S. Matz, D. Hoogestraat, V. Bhavanasi, K. Parida, K. Al-Shamery and P. S. Lee, *Adv. Mater.*, 2016, 6966–6975.
39 M. Zhang, Y. Gao, N. Chen, X. Ge, H. Chen, Y. Wei, F. Du, G. Chen and C. Wang, *Chem.–Eur. J.*, 2017, **23**, 5148–5153.
40 N. Chen, Y. Gao, M. Zhang, X. Meng, C. Wang, Y. Wei, F. Du and G. Chen, *Chem.–Eur. J.*, 2016, **22**, 7248–7254.
41 K. Saito, S. Kazama, K. Matsubara, T. Yui and M. Yagi, *Inorg. Chem.*, 2013, **52**, 8297–8299.
42 D. P. Singh, B. Sirota, S. Talpatra, P. Kohli, C. Rebholz and S. M. Aouadi, *J. Nanopart. Res.*, 2012, **14**, 781.
43 K. Hakouk, L. Lajaunie, H. El Bekkachi, B. Humbert and R. Arenal, *J. Mater. Chem. C*, 2018, **6**, 11086–11095.
44 K. Hakouk, P. Deniard, L. Lajaunie, C. Guillot-Deudon, S. Harel, Z. Wang, B. Huang, H.-J. Koo, M.-H. Whangbo, S. Jobic and R. Dessapt, *Inorg. Chem.*, 2013, **52**, 6440–6449.
45 W. Weppner and R. A. Huggins, *J. Electrochem. Soc.*, 1977, **124**, 1569.
46 E. Wenda, *J. Therm. Anal.*, 1998, **53**, 861–870.
47 X. Cui, S. H. Yu, L. Li, L. Biao, H. Li, M. Mo and X. M. Liu, *Chem.–Eur. J.*, 2004, **10**, 218–223.
48 M. Feng, M. Zhang, J. M. Song, X. G. Li and S. H. Yu, *ACS Nano*, 2011, **5**, 6726–6735.
49 C. H. B. Ng and W. Y. Fan, *Cryst. Growth Des.*, 2015, **15**, 3032–3037.
50 M. T. Fabbro, C. Saliby, L. R. Rios, F. A. La Porta, L. Gracia, M. S. Li, J. Andrés, L. P. S. Santos and E. Longo, *Sci. Technol. Adv. Mater.*, 2015, **16**, 065002.
51 F. S. Cunha, J. C. Sczancoski, I. C. Nogueira, V. G. de Oliveira, S. M. C. Lustosa, E. Longo and L. S. Cavalcante, *CrystEngComm*, 2015, **17**, 8207–8211.
52 J. V. B. Moura, J. G. Silva, P. T. C. Freire, C. Luz-lima, G. S. Pinheiro, B. C. Viana, J. M. Filho, A. G. Souza-filho and G. D. Saraiva, *Vib. Spectrosc.*, 2016, **86**, 97–102.
53 A. F. Gouveia, J. C. Sczancoski, M. M. Ferrer, A. S. Lima, M. R. M. C. Santos, M. S. Li, R. S. Santos, E. Longo and L. S. Cavalcante, *Inorg. Chem.*, 2014, **53**, 5589–5599.
54 F. D. Hardcastle and I. E. Wachs, *J. Raman Spectrosc.*, 1990, **21**, 683–691.
55 E. A. Nagul, I. D. Mckelvie, P. Worsfold and S. D. Kolev, *Anal. Chim. Acta*, 2015, **890**, 60–82.
56 J. Wang, J. Polleux, J. Lim and B. Dunn, *J. Phys. Chem. C*, 2007, **111**, 14925–14931.
57 L. Wang, S. Yan, C. D. Quilty, J. Kuang, M. R. Dunkin, S. N. Ehrlich, L. Ma, K. J. Takeuchi, E. S. Takeuchi and A. C. Marschilok, *Adv. Mater. Interfaces*, 2021, **8**, 2002080.
58 M. Grzywa, W. Łasocha and W. Surga, *J. Solid State Chem.*, 2007, **180**, 1590–1594.
59 H. Zhang, W. Wu, Q. Liu, F. Yang, X. Shi, X. Liu, M. Yu and X. Lu, *Angew. Chem., Int. Ed.*, 2021, **60**, 896–903.
60 S. C. Abrahams, *J. Chem. Phys.*, 1967, **46**, 2052.

© 2021 The Author(s). Published by the Royal Society of Chemistry

Open Access Article. Published on 13 December 2021. Downloaded on 2/20/2026 2:13:40 PM.
This article is licensed under a Creative Commons Attribution 3.0 Unported Licence.

61 O. Mtioui-Sghaier, R. Mendoza-Meroño, L. Ktari, M. Dammak and S. García-Granda, *Acta Crystallogr., Sect. E: Crystallogr. Commun.*, 2015, **71**, i6–i7.
62 T. Xiong, Y. Zhang, Y. Wang, W. S. V. Lee and J. Xue, *J. Mater. Chem. A*, 2020, **8**, 9006–9012.
63 X. He, H. Zhang, X. Zhao, P. Zhang, M. Chen and Z. Zheng, *Adv. Sci.*, 2019, 1900151.
64 V. S. Saji and C. W. Lee, *ChemSusChem*, 2012, **5**, 1146–1161.
65 X. Zhang, X. Zeng, M. Yang and Y. Qi, *ACS Appl. Mater. Interfaces*, 2014, **6**, 1125–1130.
66 Y. Liu, B. Zhang, Y. Yang, Z. Chang, Z. Wen and Y. Wu, *J. Mater. Chem. A*, 2013, **1**, 13582.
67 Y. Liu, B. H. Zhang, S. Y. Xiao, L. L. Liu, Z. B. Wen and Y. P. Wu, *Electrochim. Acta*, 2014, **116**, 512–517.
68 W. Tang, L. Liu, Y. Zhu, H. Sun, Y. Wu and K. Zhu, *Energy Environ. Sci.*, 2012, **5**, 6909.
69 F. Wang, Z. Liu, X. Wang, X. Yuan, X. Wu, Y. Zhu, L. Fu and Y. Wu, *J. Mater. Chem. A*, 2016, **4**, 5115–5123.
70 E. S. Takeuchi, A. C. Marschilok, K. Tanzil, E. S. Kozarsky, S. Zhu and K. J. Takeuchi, *Chem. Mater.*, 2009, **21**, 4934–4939.
71 A. C. Marschilok, E. S. Kozarsky, K. Tanzil, S. Zhu, K. J. Takeuchi and E. S. Takeuchi, *J. Power Sources*, 2010, **195**, 6839–6846.
72 B. Zhang, P. F. Smith, S.-Y. Lee, L. Wu, Y. Zhu, E. S. Takeuchi, A. C. Marschilok and K. J. Takeuchi, *J. Electrochem. Soc.*, 2017, **164**, A6163–A6170.
73 E. S. Takeuchi and P. Piliero, *J. Power Sources*, 1987, **21**, 133–141.
74 E. M. Sorensen, H. K. Izumi, J. T. Vaughey, C. L. Stern and K. R. Poeppelmeier, *J. Am. Chem. Soc.*, 2005, 6347–6352.
75 S. Zhang, W. Li, C. Li and J. Chen, *J. Phys. Chem. B*, 2006, **110**, 24855–24863.

© 2021 The Author(s). Published by the Royal Society of Chemistry